FMCW Radar for 3-D Tracking Based on MLBI Interferometer and MDS Estimation

Salvador Andrés, Carlos Heras, Andrés Ocabo, Jorge Lanzuela, Rubén Martínez, Asier Villafranca, Iñigo Salinas, and Rafael Alonso

***Abstract*—This article presents the implementation of a *C*-band frequency-modulated continuous wave (FMCW) radar system, utilizing software-defined radio (SDR) hardware and integrated with a five-element multilong-baseline interferometer (MLBI) receiver, for the detection and 3-D tracking of passive moving targets. A key aspect is the generation of a low jitter, high signal-to-noise-and-distortion ratio (SINAD) signal, which significantly enhances the radar's performance for angle of arrival (AoA) detection and micro-Doppler signature (MDS) estimation. The high signal quality achieved enables the detection and 3-D tracking of low radar cross-sectional (RCS) targets, such as small drones, at distances up to 800 m without requiring high radar power. In addition, this work demonstrates the effectiveness of a simple phase line assignment algorithm to mitigate errors in the AoA measurement of passive moving targets even when the MLBI geometry deviates from its optimal configuration. The performance of the radar system was evaluated in an open-field test using a DJI Mavic 3, and the results highlight the significant potential of this radar concept for medium-cost 3-D tracking and MDS identification applications.**

***Index Terms*—Angle of arrival (AoA), frequency-modulated continuous wave (FMCW), micro-Doppler signature (MDS), multilong-baseline interferometer (MLBI), radar.**

I. Introduction

FREQUENCY-MODULATED continuous wave (FMCW) homodyne radar systems have long been studied, with numerous applications, including range and speed estimation, extensively documented in the literature [1], [2]. It is well established that frequency sweep nonlinearity and local oscillator (LO) jitter significantly limit radar performance [3]. Software-defined radio (SDR) systems can potentially address some of these challenges [4], [5]. By implementing the LO through an SDR platform, high bandwidth (BW) and low jitter can be achieved, facilitating accurate range and speed estimation. These advancements have also enabled the study and analysis of the micro-Doppler signature (MDS) of the targets for their identification and characterization [6], [7], [8], [9], [10], [11], [12]. Nonetheless, these previous works either report measurements performed in laboratory conditions (a few meters range and quasi-static targets) or use expensive commercial systems with high-power and high-gain antennas.

Another important aspect of radar is the target angle estimation, which is effectively addressed in both 2-D and 3-D scenarios using techniques such as beamforming, ESPRIT, MUSIC, MVDR, and others [13], [14], [15], though their typically high cost for sub-mmWave applications limits their application range.

Tracking strategies are also well documented in the literature [16]. Recently, more affordable approaches for estimating the angle of arrival (AoA) of targets have emerged [17], [18], [19], [20]. An effective one in terms of complexity and precision is the multilong-baseline (MLBI) algorithm [20]. These techniques are optimized for specific interantenna distances and are limited in low SNR scenarios to the point where angular ambiguity correction is not possible. Also, MLBI has not yet been tested for passive moving targets, where AoA estimation is degraded by the random phase introduced by the target's shape and the relative movement of its components.

This work presents the implementation of a C-band homodyne FMCW radar system based on SDR hardware and integrated with a five-element MLBI receiver, for the detection and 3-D tracking of passive moving targets. The SDR provides low jitter and high signal-to-noise-and-distortion ratio (SINAD), which are critical for the detection of low radar cross-sectional (RCS) targets and the implementation of MLBI algorithms. In addition, we use clutter reduction [21] and time-informed clustering techniques to increase the scope of the MLBI, making it possible track of those targets.

The high signal quality and the improvement of the AoA estimation make possible detection, 3-D tracking, and MDS analysis of low RCS targets, such as small drones, at distances up to 800 m without requiring high radar power. This work also demonstrates the efficacy of a simple phase line assignment algorithm as the MLBI in field AoA measurements.

The final performance of the radar system was evaluated in a controlled open-field test using a DJI Mavic 3 drone, and the results highlight the significant potential of this radar concept for medium-cost applications.

Received 11 October 2024; revised 18 June 2025; accepted 14 August 2025. Date of publication 4 September 2025; date of current version 17 September 2025. This work was supported in part by Spanish Ministry of Science, Innovation, and Universities (MCIN)/AEI with DOI/10.13039/501100011033 under Grant DIN2021-011740 and Grant PTQ2022-012645 and in part by the INVESTIGO Program through Diputación General de Aragón (DGA) under Grant Z-0034-INVESCS-22. The Associate Editor coordinating the review process was Dr. Gang Yu. *(Corresponding author: Salvador Andrés.)*

Salvador Andrés, Andrés Ocabo, Jorge Lanzuela, and Rubén Martínez are with ZEPREN Solutions S.L., 50018 Zaragoza, Spain (e-mail: salva@zepren.com; aocabo@zepren.com; jlanzuela@zepren.com; rmartinez@zepren.com).

Carlos Heras, Iñigo Salinas, and Rafael Alonso are with the Instituto de Investigación en Ingeniería de Aragón (I3A), Universidad de Zaragoza, 50018 Zaragoza, Spain (e-mail: cdheras@unizar.es; isalinas@unizar.es; ralonso@unizar.es).

Asier Villafranca is with Alika Technologies S.L., 50018 Zaragoza, Spain (e-mail: asier@alikatechnologies.com).

Digital Object Identifier 10.1109/TIM.2025.3604971

II. Signal Description

The radar system is based on an FMCW homodyne stretch pulse compression architecture [1], [2]. The SDR generates a train of linear frequency-modulated (LFM) pulses with a pulse repetition frequency PRF. The expression for a single pulse S_{gen} is given by the following equation:

$$S_{\text{gen}} = A_{\text{gen}}\text{rect}\left[\frac{t}{t_c}\right]\cos\left(2\pi f_0 t + \frac{\text{BW}}{t_c}t^2 + \phi_{\text{gen}}\right) \quad (1)$$

where A_{gen} and φ_{gen} are the amplitude and phase of the generated signal, respectively; f_0 is the carrier frequency, t_c is the pulsewidth; and BW is the swept BW.

S_{gen} is then upconverted by a fixed factor k to generate a C-band signal of frequency kf_0. The resulting signal S_{Tx}, as shown in the following equation, is emitted by the transmitting antenna:

$$S_{\text{Tx}} = G_{\text{Tx}}\text{rect}\left[\frac{t}{t_c}\right]\cos\left(2\pi k f_0 t + k\frac{\text{BW}}{t_c}t^2 + \phi_{\text{Tx}}\right) \quad (2)$$

where G_{Tx} is the amplitude of the transmitted signal after the amplification stage and φ_{Tx} is the corresponding phase.

The received target echo signal S_{Rx} is a reflected, attenuated, and time delayed copy of the transmitted signal as described in (3). The time delay τ of the received signal depends on the target speed v_r and its original distance R_0, as indicated in (4). The amplitude of the received signal G_{Rx} depends on the emitted power and the target RCS and distance as described by the well-known radar equation [1]

$$S_{\text{Rx}} = G_{\text{Rx}}\text{rect}\left[\frac{t-\tau}{t_c}\right] \times \cos\left[2\pi\left(kf_0(t-\tau) + k\frac{\text{BW}}{t_c}(t-\tau)^2\right) + \phi_{\text{Rx}}\right] \quad (3)$$

$$\tau = \frac{2R_0}{c} + \frac{2v_r t}{c}. \quad (4)$$

In our homodyne architecture, S_{Tx} is used as the reference waveform or LO [1]. Since $\tau \ll t_c$ for the instrument range, it is not necessary to introduce a time delay for the reference signal.

The process of mixing the received signal with the LO, known as the deramping process, generates an upper sideband signal, which is rejected by a bandpass filter (BPF) and a lower sideband sinusoidal signal S_{Mx} [1], [2], as shown in the following equation:

$$S_{\text{Mx}} = G_{\text{BB}}\text{rect}\left[\frac{t}{t_c}\right]\text{rect}\left[\frac{t-\tau}{t_c}\right]\cos\left[2\pi(f_b t) + \theta\right] \quad (5)$$

where G_{BB} is the baseband amplitude, f_b is the beat frequency (6), and θ is the carrier phase shift term (7)

$$f_b = k\frac{\text{BW}}{t_c}\tau \quad (6)$$

$$\theta = 2\pi k f_0 \tau - 2\pi k\frac{\text{BW}}{t_c}\tau^2. \quad (7)$$

Under the assumption of slow-motion targets, f_b and R_0 remain constant for a small number N of subsequent chirps. Nevertheless, the carrier term kf_0 in θ causes a slight shift in the phase of S_{Mx} over time due to v_r.

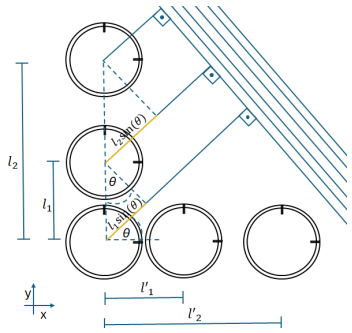

Fig. 1. 3-D phase interferometer of a five-element array.

The peak of the 2-D fast Fourier transform (FFT) of S_{Mx} contains the range and velocity information of the target. The result of the 2-D FFT is called the range–Doppler map. The first FFT, known as range FFT, is performed over the sampled signal during t_c at a sampling frequency f_{sample}. Also, the second FFT, known as the Doppler FFT, is performed for each range over the chirp frame of N chirps at sampling frequency equal to the PRF, giving the phase shift in S_{Mx}.

The sampling processes at f_{sample} and PRF produce aliasing if the Nyquist criterion is not met [1]. For a BW of $f_{sample}/2$ and PRF/2, an unambiguous range R_{un} and an unambiguous speed V_{un} are defined as follows:

$$R_{\text{un}} = \frac{c \cdot t_c \cdot f_{\text{sample}}}{4k \cdot \text{BW}} \quad (8)$$

$$V_{\text{un}} = \frac{c \cdot PRF}{4k \cdot f_0}. \quad (9)$$

The Rayleigh criterion for discrete time signals [2] establishes a Rayleigh range resolution given by (10) and analogously a Rayleigh speed resolution given by (11)

$$\delta R = \frac{c}{2k \cdot \text{BW}} \quad (10)$$

$$\delta V = \frac{\mathbf{c}}{2k \cdot f_0}\frac{PRF}{N}. \quad (11)$$

If δV is small enough, each moving part of the target with a speed of $v_r + \varepsilon_i$ has a time delay τ_i, as shown in (12). The superposition of the signals generated by the main body of the target and the independently moving parts is the MDS of the target

$$\tau_i = \frac{2R_0}{c} + \frac{2(v_r + \varepsilon_i)t}{c} \quad (12)$$

where ε_i is the small difference between the speed of the main body v_r and the speed of the moving part.

The concept of the MLBI with a five-antenna 2-D array in an L configuration—comprising three antennas for the horizontal array and three antennas for the vertical array with a common reference antenna—is shown in Fig. 1. When an antenna array, for example vertical one in the figure, is used to capture the reflected signal from a target subtending a nonzero solid angle, phase differences arise between the antennas due to their spatial separation l_1 and l_2, as described in (13).

These phase differences ϕ_i are defined for each auxiliary antenna $i = 1, 2$ with respect to the phase of the reference antenna. Using ϕ_1 and ϕ_2, the AoA of a target with respect to the normal direction of the antenna array θ is calculated

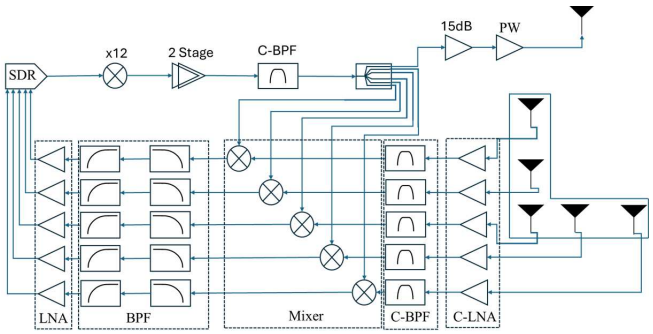

Fig. 2. Radar schematic.

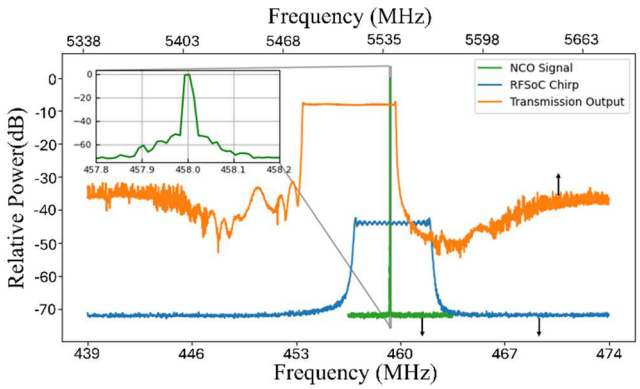

Fig. 3. SDR-generated tone (green, bottom axis), SDR-generated chirp (blue, bottom axis), and the output of the generation branch (orange, top axis).

using (14). When the condition of $\phi_i < \pi$ is matched ($l_i < \lambda$), there is no ambiguity in θ. However, when $\phi_i > \pi$, there is θ ambiguity that needs to be resolved. On the other hand, the raw phase error of θ, denoted as σ_θ, decreases with the distance between antennas l_2 as shown in (15). Hence, there is a tradeoff between ambiguity and the raw phase error with l_2 in the antenna array design

$$\phi_i = 2\pi \frac{R_0 \sin(\theta)}{\lambda} + n_i 2\pi \tag{13}$$

$$\theta = \arcsin\left(\frac{\lambda \phi_2}{2\pi l_2}\right) \tag{14}$$

$$\sigma_\theta = \frac{\lambda}{\sqrt{\text{SNR}} \cdot 2 \cdot \pi \cdot l_2 \cdot \cos(\theta)} \tag{15}$$

where $n_i \in N$ represents the number of rotations above 2π.

To deal with the ambiguity in the case of $l_i > \lambda$ of several MLBI algorithms have been presented in the literature. We implement the one proposed by Van-Sang Doan et al. [20], in which the array is designed with the configuration (0, X, and Y)$\lambda/2$, where $X, Y \in \mathbb{N}$, and $X < Y$. X and Y have the greatest common divisor equal to 1. Then, the relation between the phase differences ϕ_1 and ϕ_2 is derived from (13) to (15)

$$\phi_2 = \frac{X}{Y}\phi_1 + 2\pi\left(\frac{Xn_1 - Yn_2}{X}\right). \tag{16}$$

According to Doan et al. [20], a suitable X:Y ratio is 3:4 for a three-element array. When the antenna array is not optimized with this ratio, the line pattern generated by (16) becomes denser, and resolving the ambiguity requires additional algorithm effort, as described in Section IV.

III. Radar Scheme

The schematic of the radar is shown in Fig. 2. The system uses a field-programmable gate array (FPGA)-based SDR, an upconversion stage, a power amplification transmission branch, and five reception branches with corresponding down-conversion stages and baseband signal amplification.

The SDR is part of the RFSoC Gen3 family. This family is required for high data rate and parallelism in combination with low noise floor and jitter in radio frequency (RF) signal generation. The SDR integrates 12-bit 4.91-gigasamples per second (GSPS) analog-to-digital and digital-to-analog converters (ADC and DAC), an internal numerically controlled oscillator (NCO), and a $x24$ decimation FIR filter. Although the generated and acquired signals are confined to the UHF band, the requirements of image rejection for high-quality signal generation, multitile synchronization (MTS) for inter-channel synchronization, data exchange into and out of the SDR, and oversampling during acquisition to suppress aliasing from residual power supply and other noise sources necessitate the use of a gigahertz-range system clock. The signal generated by the DAC is an LFM signal as (1) with a BW of 5 MHz. It is multiplied by the FPGA internal NCO to move it to the UHF band. This signal has 71 dB of SINAD and 0.15-MHz jitter. The SDR chirp signal is broadened and frequency shifted by a factor $k = 12$ as (2) by Mini Circuits Model ZX90-12-63-S+ with 8-dB conversion losses, resulting in a C-band signal with 60 MHz of BW. The C-band signal is amplified by a two-stage process.

A BPF is used to eliminate harmonics and low-frequency modulation of the baseband signal. Fig. 3 shows the measured 458-MHz tone generated by the SDR platform, the SDR-generated chirp, and the transmission branch output signal. The filtered signal is split with a six-way splitter to generate the five LO signals for the reception branches and the signal for the transmit branch. It ensures coherence between them so that received signals can be used in the angle estimation for the tracking algorithms and redundancy between them for clustering and error correction.

The transmission branch presents an additional gain preamplifier to accommodate the input signal of the power amplifier (PW).

The MLBI antenna array consists of five identical antenna elements, Ubiquiti PrismAP-5-90, built in an L-shape. The X: Y values are limited by the antenna element geometry, and the closest possible values to the optimum ratio are chosen, 6:13 for azimuth and 7:15 for elevation.

Each reception branch implements a C-band low noise amplifier (LNA) and a second-order flat response C-band filter. The received signals are mixed with their corresponding LO signals as described in (5). The resulting baseband signals have different artifacts due to interference, harmonics, and mixing crosstalk. These artifacts can be partially removed by bandpass filtering since the range under study is known. The five reception branches are connected to a multichannel FPGA-based SDR platform using MTS. Constant phase offsets between channels, resulting from differences in electrical path lengths, are compensated during the angle calibration process.

TABLE I
SYSTEM PARAMETERS

Parameter	Value
Frequency	C band
Azimuth & elevation coverage	90º & 45º
PRF	1.7 kHz
Instrument range	1 km for 0.01RCS
Output peak power	50 W
Range-Doppler map noise floor	-100 dBm
Range & speed resolution (10)(11)	2.5m & 0.7 or 0.2 m/s
Unambiguous range & speed (8)(9)	10km & 84km/h
Azimuth & elevation max. error (º)	±1 & ±1.5 at 700m in 0º

Fig. 4. Radar system installation.

Frequency spectra are computed by the FFT Xilinx IP Core after data accommodation and interchannel signal synchronization. The signals are acquired simultaneously across the five channels. A 2-D FFT is applied for each channel to obtain R_0 and v_r as shown in (4), (6), and (7).

In this implementation, the selected sampling frequency after the $x24$ decimation FIR filter is 204 MSPS with a 41-μs chirp time. It assures at least ten data points to extract correctly the phase in a range of 1 km or f_b = 10 MHz (6). The 60-MHz BW ensures a range resolution of 2.5 m (10). The 1/PRF is selected to 0.6 ms for a maximum speed of 84 km/h (9) and the chirp frame is 64 or 256 for a speed resolution of 0.7 or 0.2 m/s (11).

The system parameters are presented in Table I. The simulated angle error, according to [20], for the conditions described in Table I, is close to 0.5° for 8-dB SNR, but the experimental 3σ error obtained in the field test is larger due to the impossibility of using the optimal design ratios for the antenna array.

IV. EXPERIMENTAL RESULTS

The radar system was deployed in a testing ground, as shown in Fig. 4, for range, AoA, and 3-D tracking. The test was carried out with a Mavic 3 drone as the target.

The range test was conducted using forward and backward drone flights over a distance of 1 km following the normal direction to the antenna array plane. This trajectory is also used to calibrate the zero angle and the σ_θ dispersion over

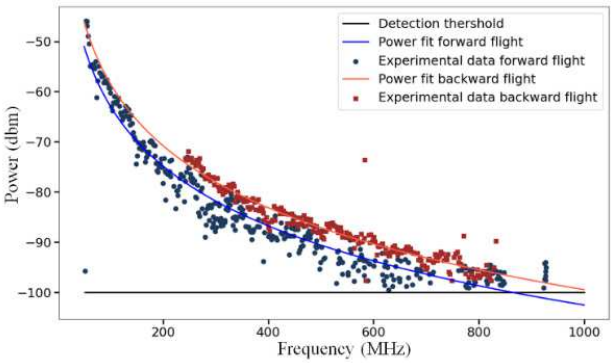

Fig. 5. Range test results.

the distance for the AoA algorithms. The results are shown in Fig. 5. The black solid horizontal line indicates the detection umbral of the radar system. The circles represent a forward flight, while the squares represent a backward flight. Both traces align with the expected logarithmic decay with the distance R_0, power $\approx -4\log(R_0)$, and show a power dispersion across the theoretical plot due to variations in the drone's tilt along its flight. The forward flight reports 5 dB more detected power than the backward flight due to the differing RCS of the front and rear faces of the drone.

The AoA test was conducted with vertical (30° elevation angle range in a forward trajectory) and horizontal (70° azimuth angle range in a forward trajectory) drone flights. As described in the previous section, ϕ_1 and ϕ_2 data are measured for each chirp frame.

The measured ϕ_2 is used to obtain AoA by using (13), while ϕ_1 disambiguates the n_2 index in ϕ_2. Red points on Fig. 6(a) and (d) represent the relationships of the raw measured (ϕ_1, ϕ_2) data in the elevation and azimuth tests, respectively. In the figures, blue lines represent the ideal line pattern of the relationships of (ϕ_1, ϕ_2) obtained from (16) for a ±90° angle range and the specified X:Y ratio. It is noted that the line numbers in the phase plane correspond to the coefficient n_2. The red lines indicate the unambiguity limit, which is half the distance between neighboring ideal phase lines. As we are tracking a moving target, measured (ϕ_1, ϕ_2) data must be positioned in the ideal lines in a specific sequence of n_2 index as the AoA varies with time across the drone trajectory. Nevertheless, many of the (ϕ_1, ϕ_2) data have significant raw phase errors due to target-induced phase changes, clutter, interference or system noise. It results in measured values (ϕ_1, ϕ_2) that deviated from the ideal line. In these cases, we need to find the nearest ideal line to this point (ϕ_1, ϕ_2) to determine n_2 (corresponding to the actual phase difference ϕ_2) without ambiguity with the neighboring ideal line.

We implement a phase line assignment algorithm that is based on the method proposed by Van Doan et al. [20], and which incorporates an additional, straightforward algorithm based on clustering and target designation to address moving targets. The algorithm considers the measured distances and speeds in each timestamp of a target across its tracking. First, the phase plane and measured (ϕ_1, ϕ_2) points are rotated about the angle $\alpha = a\tan(\text{X/Y})$ as (17) to ensure that the phase lines

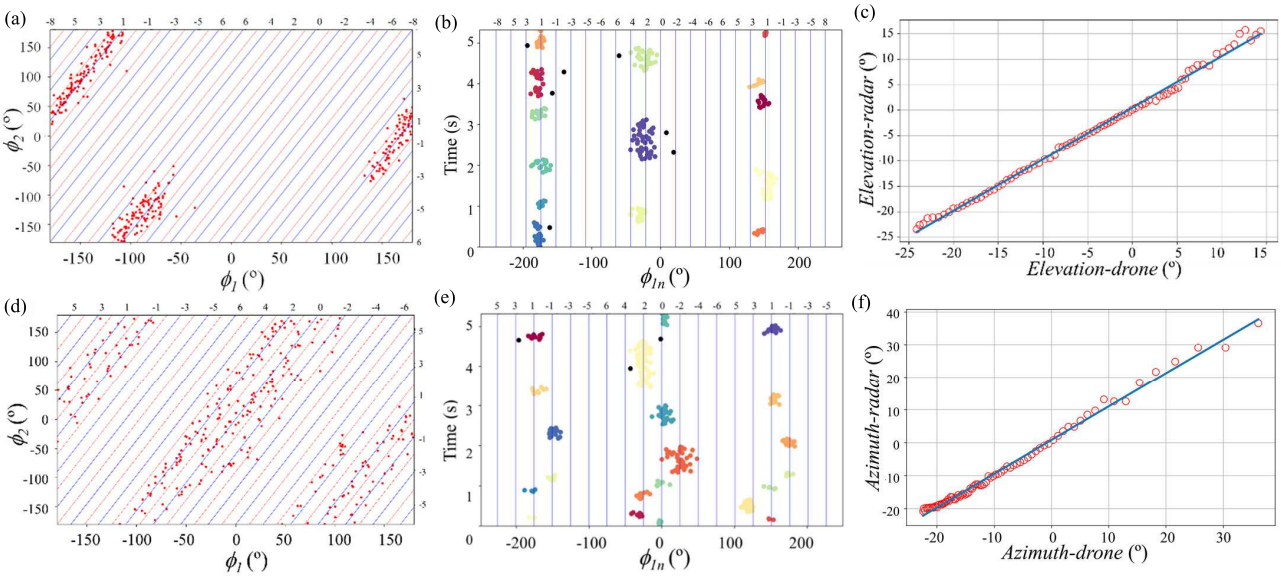

Fig. 6. (a) MLBI phase plane in the elevation test. (b) $\phi_{1n}(t)$ data in the elevation test. (c) Elevation test. (d) MLBI phase plane in the azimuth test. (e) $\phi_{1n}(t)$ data in the azimuth test. (f) Azimuth test.

are perpendicular to the horizontal axis

$$\begin{bmatrix} \phi_{1n} \\ \phi_{2n} \end{bmatrix} = \begin{bmatrix} \cos\alpha & -\text{sen}\alpha \\ \text{sen}\alpha & \cos\alpha \end{bmatrix} \text{x} \begin{bmatrix} \phi_1 \\ \phi_2 \end{bmatrix}. \quad (17)$$

It results in (ϕ_{1n}, ϕ_{2n}) points. In Fig. 6(b) and (e), we represent the ϕ_{1n} values with the time in the elevation and azimuth tests. Note that, ϕ_{1n} is a linear combination of both ϕ_1 and ϕ_2. As we track a moving target, the ϕ_{1n} points traverse the ideal lines in a linear sequence of n_2. The algorithm clusters them by proximity, which is represented in the figures by different color; black color is used for unclustered values, which are rejected. The center of mass of each designed cluster is computed. Then, each measured point ϕ_{1n} of the same cluster approaches the nearest neighboring phase of its center of mass. Each ϕ_{1n} value now becomes an address index n_2, and AoA is calculated with (13). Finally, the algorithm evaluates that the evolution of the AoA over multiple consecutive frames is consistent with the smooth and continuous time evolution of the measured distances and speeds, and only those points that fall within a margin of validity are considered correct.

Fig. 6(c) and (f) represents the radar measured AoA with respect to the angles provided by the drone's global navigation satellite system (GNSS) during the elevation and azimuth tests, respectively. A linear fit is performed on both traces in both cases. We can observe that the zero angle calibration is well executed that the angles are accurately resolved across the entire range, except in the final part of the trajectories, which corresponds to the farthest segment with the poorest SNR and lower point density for the clustering. Note that, the density of measurement points is higher when the drone's flight path is close to the radar, as the angular change is greater with the distance traveled. Conversely, when the drone follows a trajectory farther from the radar, the angular variation is smaller with the distance traveled. The maximum AoA error (Table I) obtained using the proposed phase line assignment algorithm, with a nonoptimal interantenna spacing ratio of 6:13 in azimuth and 7:15 in elevation, outperforms those reported

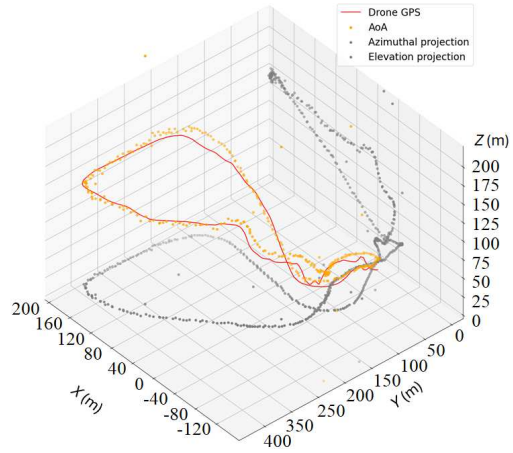

Fig. 7. Reconstructed 3-D trajectory of a drone's flight.

for generic MIMO (4.1° at 2 km) [14] and MUSIC (1° at meters) [15], and is comparable to the MLBI method [20], with a 3:4 optimal interantenna ratio and four receiving elements.

A 3-D trajectory of the drone, reconstructed from the radar measured range, azimuth, and elevation data, is compared with the drone's own GNSS data in Fig. 7. The radar data are represented by orange dots, while the drone's GNSS data are shown as a solid red line. Gray points represent projections of the radar data to the azimuth and elevation planes.

In the presence of clutter or multipath signals, the MLBI algorithm is able to resolve the angle, making tracking possible, if the power ratio between clutter and signal is lower than 0.2, as stated in [20]. The study of tracking for sparse multitarget scenarios is beyond the scope of this article.

The Doppler FFT can also be applied at any segment of the measured trajectory to obtain the instant speed of the drone and thanks to the accuracy and resolution achieved in the radar signals, the MDS of the drone can be seen.

Fig. 8 represents the measured speeds in the backward flight segment for 64 chirps per frame in Fig. 8(a) and 256 chirps in

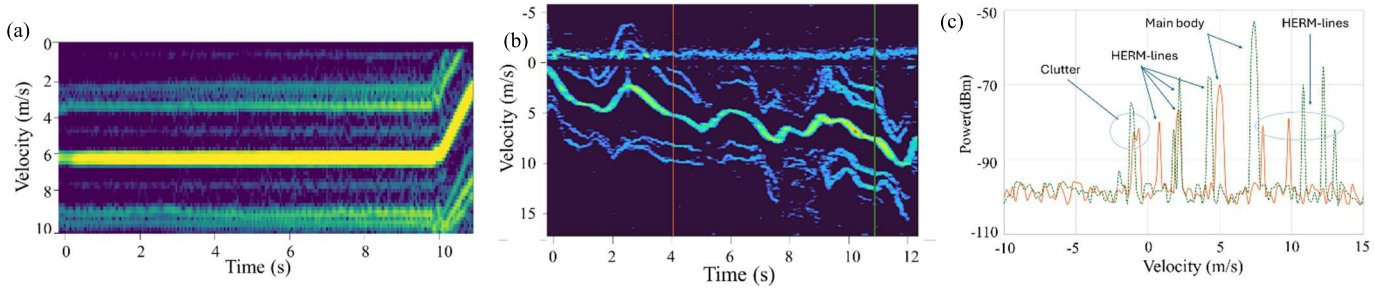

Fig. 8. MDS drone signatures. (a) 64 chirps per frame. (b) 256 chirps per frame. (c) Doppler FFT of two timestamps of (b). Green and orange lines indicate the corresponding timestamps in (b) of the orange and doted green traces in (c).

Fig. 8(b) and (c). Speeds are represented in a heatmap, indicating the power of each of the resolved Doppler frequencies in a greenish-blue to red color gradient. The yellow trace in Fig. 8(a) and the cyan trace in Fig. 8(b) correspond to the main body of the drone. The modulation from the drone's propellers, represented as helicopter rotor modulation (HERM) lines, is visible as parallel cyan lines in Fig. 8(b) and greenish-blue traces in Fig. 8(a), both aligned with the central body trace.

The presence of four HERM lines is consistent with the four propellers of the Mavic 3 model. A higher Doppler FFT resolution, achieved by processing 256 chirps per frame, is demonstrated in Fig. 8(b) for a nonuniform drone flight, providing clearer details of the HERM lines. In this figure, the temporal evolution of the propellers' modulation lines can be observed, corresponding to the accelerations and decelerations necessary to stabilize the drone's flight. Fig. 8(a) illustrates that the HERM lines are still discernible even with fewer chirps per frame, although the capacity for detailed analysis of the propeller dynamics is reduced. However, the system retains sufficient resolution for target discrimination, requiring significantly fewer system resources.

The 0.2-m/s velocity resolution obtained in these results is similar to that reported in recent publications either in laboratory conditions and short range [6], [7], [8], [9] or using commercial radar systems with medium power (2 kW) and high-gain antennas (2° conical aperture) for km range [10], [11], [12]. Our system achieves MDS signals comparable to those, while using low-power (50 W) and low-gain antennas (45° elevation and 90° azimuthal aperture) for a 1-km range.

By integrating MDS pattern analysis with trajectory analysis, the system can more effectively identify potential target types, including drones, birds, and bats. By leveraging machine learning techniques or statistical models implemented in an FPGA, the classification can be optimized for real-time identification, enhancing the system's ability to differentiate between similar targets and improving detection accuracy in diverse environmental conditions.

V. Conclusion

We have presented the implementation of a C-band FMCW radar system utilizing SDR hardware and integrated with a five-element MLBI receiver for detection, 3-D tracking, and MDS measurement of passive moving targets. The high signal quality achieved with the SDR enables 3-D tracking and classification of low RCS targets, such as small drones, at distances up to 800 m, without requiring high radar power. This work also demonstrates the effectiveness of a simple phase line assignment algorithm in mitigating errors in the AoA measurement of passive moving targets, even when the antenna array geometry deviates from the optimal configuration. The radar performance has been evaluated in an open-field test using a DJI Mavic 3, and the results highlight the significant potential of this radar concept for medium-cost 3-D tracking and MDS identification applications.

References

[1] M. I. Skolnik, *Radar Handbook*, M. R. Ducoff and B. W. Tietjen, Eds., New York, NY, USA: McGraw-Hill, 2008, ch. 8.

[2] W. L. Melvin, *Principles of Modern Radar: Advanced Techniques*, B. Murray and J. Mike, Eds., Rijeka, Croatia: SciTech, 2012, ch. 2.

[3] Z. Ali et al., "Impact of receiver thermal noise and PLL RMS jitter in radar measurements," *IEEE Trans. Instrum. Meas.*, vol. 73, pp. 1–10, 2024, doi: 10.1109/TIM.2024.3370745.

[4] W. Feng, J. -M. Friedt, and P. Wan, "SDR-implemented ground-based interferometric radar for displacement measurement," *IEEE Trans. Instrum. Meas.*, vol. 70, 2021, Art. no. 8502218, doi: 10.1109/TIM.2021.3069805.

[5] G. C. George, J. J. U. Buch, A. Prince, and S. K. Pathak, "SoC-based automated diagnostic instrument for FMCW reflectometry applications," *IEEE Trans. Instrum. Meas.*, vol. 70, 2021, Art. no. 2004411, doi: 10.1109/TIM.2021.3078505.

[6] J.-S. Suh, L. Minz, D.-H. Jung, H.-S. Kang, J.-W. Ham, and S.-O. Park, "Drone-based external calibration of a fully synchronized Ku-band heterodyne FMCW radar," *IEEE Trans. Instrum. Meas.*, vol. 66, no. 8, pp. 2189–2197, Aug. 2017, doi: 10.1109/TIM.2017.2687518.

[7] K.-B. Kang, J.-H. Choi, B.-L. Cho, J.-S. Lee, and K.-T. Kim, "Analysis of micro-Doppler signatures of small UAVs based on Doppler spectrum," *IEEE Trans. Aerosp. Electron. Syst.*, vol. 57, no. 5, pp. 3252–3267, Oct. 2021, doi: 10.1109/TAES.2021.3074208.

[8] J. Gong, J. Yan, D. Li, R. Chen, F. Tian, and Z. Yan, "Theoretical and experimental analysis of radar micro-Doppler signature modulated by rotating blades of drones," *IEEE Antennas Wireless Propag. Lett.*, vol. 19, no. 10, pp. 1659–1663, Oct. 2020, doi: 10.1109/LAWP.2020.3013012.

[9] C. Clemente et al., *All Radar Countermeasures for Unmanned Aerial Vehicles*, M. Ritchie et al., Eds., Rijeka, Croatia: SciTech, 2021, ch. 9.

[10] D. White, M. Jahangir, J. P. Wayman, S. J. Reynolds, J. P. Sadler, and M. Antoniou, "Bird and micro-drone Doppler spectral width and classification," in *Proc. 24th Int. Radar Symp. (IRS)*, Berlin, Germany, May 2023, pp. 1–10, doi: 10.23919/IRS57608.2023.10172408.

[11] B. I. Ahmad and S. Harman, "Tracking of target body and micro-Doppler components in drone surveillance radar," in *Proc. Int. Conf. Radar Syst. (RADAR)*, vol. 2022, Oct. 2022, pp. 260–265, doi: 10.1049/icp.2022.2327.

[12] M. Jahangir et al., "Networked staring radar testbed for urban surveillance: Status and preliminary results," in *Proc. Int. Conf. Radar Syst. (RADAR)*, Edinburgh, U.K., Oct. 2022, pp. 471–476, doi: 10.1049/icp.2022.2363.

[13] A. M. Molaei, B. Zakeri, S. M. H. Andargoli, M. A. B. Abbasi, V. Fusco, and O. Yurduseven, "A comprehensive review of direction-of-arrival estimation and localization approaches in mixed-field sources scenario," *IEEE Access*, vol. 12, pp. 65883–65918, 2024.

[14] S. Saponara and B. Neri, "Radar sensor signal acquisition and multidimensional FFT processing for surveillance applications in transport systems," *IEEE Trans. Instrum. Meas.*, vol. 66, no. 4, pp. 604–615, Apr. 2017, doi: 10.1109/TIM.2016.2640518.
[15] C. Codău, R.-C. Buta, A. Păstrăv, P. Dolea, T. Palade, and E. Puschita, "Experimental evaluation of an SDR-based UAV localization system," *Sensors*, vol. 24, no. 9, p. 2789, Apr. 2024, doi: 10.3390/s24092789.
[16] B. P. Gibbs, "Advance Kalman filtering," in *Least-Squares and Modeling: A Practical Handbook*. Hoboken, NJ, USA: Wiley, 2011.
[17] H. Chen, T. Ballal, and T. Y. Al-Naffouri, "DOA estimation with non-uniform linear arrays: A phase-difference projection approach," *IEEE Wireless Commun. Lett.*, vol. 10, no. 11, pp. 2435–2439, Nov. 2021, doi: 10.1109/LWC.2021.3102402.
[18] X. Tran, T. Nguyen, J. Vesely, F. V. Dvorak Minh Duong, and V. Doan, "Optimization of non-uniform planar antenna array topology in two-dimensional DOA estimation," *Adv. Mil. Technol.*, vol. 15, no. 2, pp. 393–403, Dec. 2020, doi: 10.3849/aimt.01389.
[19] E. J. Holder, *Angle of Arrival Estimation Using Radar Interferometry: Methods and Applications*. Stevenage, U.K.: IET Digital Library, doi: 10.1049/SBRA508E.
[20] V.-S. Doan, T. The, V.-P. Hoang, and J. Vesely, "Phase-difference measurement-based angle of arrival estimation using long-baseline interferometer," *IET Radar, Sonar Navig.*,, vol. 17, no. 3, pp. 449–465, doi: 10.1049/rsn2.12352.
[21] Q. Zheng et al., "A target detection scheme with decreased complexity and enhanced performance for range-Doppler FMCW radar," *IEEE Trans. Instrum. Meas.*, vol. 70, 2021, Art. no. 8001113, doi: 10.1109/TIM.2020.3027407.

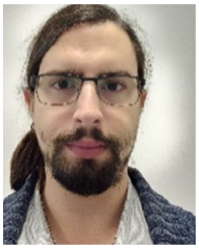

Salvador Andrés received the B.Sc. degree in physics and the M.Sc. degree in telecommunications engineering from the University of Zaragoza, Zaragoza, Spain, in 2019 and 2023, respectively, where he is currently pursuing the Ph.D. degree in telecommunications engineering.

He is currently employed at ZEPREN Solutions S.L., Zaragoza, where he is engaged in the research and development.

Carlos Heras received the M.Sc. degree in physics from the University of Zaragoza, Zaragoza, Spain, in 1994, and the Ph.D. degree in physics studying optical fiber nonlinearities and their effects and applications in optical communications from the University of Zaragoza, in 2003.

In 2004, he joined the University of Zaragoza, Zaragoza, as an Assistant Professor. He became an Associate Professor, in 2008.

Dr. Heras is a member of the Photonics Technology Group.

Andrés Ocabo received the B.Sc. and M.Sc. degrees in telecommunications engineering from the University of Zaragoza, Zaragoza, Spain, in 2019 and 2021, respectively.

He currently works as the Project Manager at ZEPREN Solutions S.L., Zaragoza, specializing in radar and fiber-optic sensing technologies in sectors such as automotive and renewable energy. He has over four years of experience as a signal processing and data analysis engineer.

Jorge Lanzuela received the M.Sc. degree in telecommunications engineering from the University of Zaragoza, Zaragoza, Spain, in 2022.

After participating in research projects related to radar, electronics, and photonics at the Photonic Technologies Group, University of Zaragoza, he joined ZEPREN Solutions S.L., Zaragoza, as a Research and Development Engineer. At ZEPREN Solutions S.L., he has continued to work on various projects related to optical communications, renewable energies, and radar technologies.

Rubén Martínez received the bachelor's degree in physics and the M.Sc. degree in physics and physical technologies from the University of Zaragoza, Zaragoza, Spain, in 2011 and 2012, respectively, and the Ph.D. degree from the University of Valencia, Valencia, Spain, in 2018.

He worked as an Optical Engineer at HP, Sant Cugat del Vallés, Barcelona, Spain, and Ficosa, Viladecavalls, Barcelona, Spain, from 2017 to 2019, the Project Manager at Aragon Photonics Laboratory, Zaragoza, from 2020 to 2021, and Circe Foundation in 2022. Since 2023, he has been the Project Manager at ZEPREN Solutions S.L., Zaragoza.

Asier Villafranca received the M.Sc. degree in telecommunications engineering and the Ph.D. degree from the University of Zaragoza, Zaragoza, Spain, in 2004 and 2009, respectively.

From 2005 to 2011, he worked as a Researcher at the University of Zaragoza, and the CTO at Aragon Photonics Laboratory, Zaragoza, from 2011 to 2021. Since 2021, he has been the CTO at Alika Technologies S.L., Zaragoza. His research revolves around test and measurement methods.

Iñigo Salinas received the M.Sc. degree in physics and the Ph.D. degree from the Sciences Faculty, University of Zaragoza, Zaragoza, Spain, in 1996 and 2003, respectively.

He is currently an Associate Professor with the Electrical Engineering and Communications Department, University of Zaragoza. His main research interests are optical characterization, instrumentation, and multilayers.

Dr. Salinas is a member of the Photonics Technologies Group at the Aragon Institute for Engineering Research (I3A).

Rafael Alonso received the M.Sc. and Ph.D. degrees in physics from the University of Zaragoza, Zaragoza, Spain, in 1988 and 1995, respectively.

He is with the Department of Applied Physics, University of Zaragoza, where he is currently a Professor. His research interests include the fields of optical fiber devices, electromagnetic characterization, optoelectronic instrumentation, and radar technologies.

Dr. Alonso is a member of the Aragon Institute for Engineering Research (I3A).